Research article

Shaimaa I. Azzam* and Alexander V. Kildishev*

Time-domain dynamics of reverse saturable absorbers with application to plasmon-enhanced optical limiters

https://doi.org/10.1515/nanoph-2018-0139
Received September 7, 2018; revised October 27, 2018; accepted October 30, 2018

Abstract: An advanced full-wave time-domain numerical model for reverse saturable absorption (RSA) is presented and verified. Rate equations describing atomic relaxations and excitation dynamics are coupled to the Maxwell equations by using a Lorentzian oscillator, which models the kinetics-dependent light–matter interactions. The presented novel technique provides a versatile multiphysics framework for designing complex structures and integrating diverse material models that were not previously possible. The multiphysics framework allows capturing the behavior of the RSA materials embedded in artificial photonic nanostructures that cannot be analyzed with established techniques such as the Beer–Lambert law. To showcase the importance of the full-wave RSA analysis coupled to carrier kinetics, we analyze two plasmon-enhanced optical limiters: a metal grating and a Fabry–Perot cavity-like structure where we decrease the unenhanced limiter threshold by a factor of 3 and 13, respectively. This is a promising approach for developing RSA devices operating at reduced illumination levels and thereby significantly expanding their area of applicability to areas such as protective eyewear and automatically dimmed windows. By exploring the dynamic behavior of a given RSA system, this framework will provide critical insights into the design of transformative photonic devices and their complementary optical characterization, and serve as an invaluable utility for guiding the development of synthetic absorbing materials. We believe that our multiphysics models are crucial enabling tools that lay a necessary foundation for the numerical machinery required for the realization and optimization of optical limiting and all-optical switching systems.

Keywords: optical limiters; reverse saturable absorption; multilevel system; rate equations; nonlinear plasmonics.

***Corresponding authors: Shaimaa I. Azzam and Alexander V. Kildishev,** School of Electrical and Computer Engineering, and Birck Nanotechnology Center, Purdue University, West Lafayette, IN 47907, USA, e-mail: sazzam89@gmail.com (S.I. Azzam); kildishev@purdue.edu (A.V. Kildishev).
https://orcid.org/0000-0002-4319-3813 (S.I. Azzam),
https://orcid.org/0000-0002-8382-8422 (A.V. Kildishev)

1 Introduction

There has been renewed interest in the optical community to protect optical sensors and, more importantly, human eyes from accidental or intentional harm caused by high-intensity light sources. This is accomplished by optical limiters (OLs), which have low absorption at low light intensities and high absorption at higher intensities. Multiple nonlinear processes could be utilized for optical limiting, including nonlinear scattering, absorption, refraction, and multiphoton absorption [1]. Materials exhibiting nonlinear absorption, specifically reverse saturable absorption (RSA), are among the most popular for OLs [1]. RSA materials provide high transmission (low absorption) at low intensity of incident light, and low transmission when the intensity of incident light becomes high. Defined more rigorously, RSA occurs when the absorption cross-section of the excited states is larger than that of the ground states. RSA also requires the lifetime of the triplet state to be relatively long, which is reflected directly in the efficiency and the saturation intensity of the OL. The wide range of materials that exhibit RSA includes metals [2], organic dyes [3, 4], clustered metal particles [5, 6], synthetic compounds [7], carbon nanotubes [8], and two-dimensional materials [9, 10].

Unlike other nonlinear phenomena, there are surprisingly few efforts to develop complete multiphysics models of optical limiting devices based on RSA with resonant nanostructured optical elements. Such models would allow significant improvement of the size, weight, and power metrics of this class of OLs. One of the most sought-after requirements is obtaining RSA at normal

illumination levels, which would greatly expand their area of applicability such as protective eyewear and automatically dimmed windows [11, 12] and open up new opportunities for obtaining high-RSA materials at weak, incoherent light. Most RSA materials have extremely high saturation energies, defined as the energy required to reduce the linear transmittance to 1/e of its linear value. This limits the use of OLs based on those materials to very intense and/or very short laser pulses. Current efforts to optimize optical limiting properties are material-focused. Using material synthesis, chemical engineering, and functionalization of materials to increase their triplet state lifetime have been widely explored to get enhanced RSA characteristics at the power level of sunlight [11, 12]. We believe that a critical limiting factor hindering the optimization and enhancement of OLs at the device level is the lack of material models that account for the quantum mechanical origin of RSA and its relevant representation in the time domain. Once an accurate model of RSA is available, boosting the performance of OLs using the current advances in nanophotonics and micro- and nanofabrication should be made substantially more achievable. Thus far, there have been efforts to model saturable nonlinearities in the time domain using various methods such as a saturable harmonic oscillator [13] as well as two-level systems for saturable absorbers [14, 15]. For RSA, the physical mechanism causing the absorption is somewhat more involved and requires taking into account different timescales as well as the absorption contributions of both the singlet and triplet states.

In this work, we propose an advanced time-domain numerical simulation approach that models the RSA process as an atomic multilevel system in a 3D full-wave multiphysics framework. We integrate our material model as a proprietary ADE (application domain extension) code in a commercial-grade solver based on the 3D finite-difference time-domain method. This approach allows expanding the versatility of target problems through the advanced pre- and post-processing features of the commercial solver [16]. With this approach, we can simulate the different relaxations taking place in the material and get an idea of how they affect the nonlinear optical material response. Additionally, we can also realize a deeper understanding of the excitation mechanisms, and then employ this comprehensive knowledge to optimize optical limiting devices and systems. Similar to the experiment-fitted time-domain kinetic models of gain media [17], feedback from optical experiments should always be recommended for accurate material modeling in the design and optimization of real-life RSA devices. Advantages of our scheme include (i) self-consistent description of the excitation and relaxations dynamics, coupled to (ii) 3D full-wave multiphysics environment with the geometry discretization that can handle an arbitrary structural complexity, and accurately model focused/structured beams that match experimentallyused sources, without resorting to paraxial or non-paraxial approximations, and, finally, (iii) in-depth post-processing of the simulated data – time-resolved tracking of *E*-fields, polarizations, and population kinetics – getting physical insights into the system dynamics not otherwise available through experiment. Moreover, we use our multiphysics framework to design the plasmon-enhanced OL devices with an order of magnitude reduction in the saturation intensity. This is a critical improvement that brings the activation energies of the OLs to reduced illumination levels, thus significantly expanding the area of application for these devices. Following this introduction, a particular topology of a multilevel atomic system for modeling RSA is introduced and explained with more details in Section 2. Then, the numerical framework and results obtained from the discretized models are discussed in Section 3. Time dynamics of the system along with the effects of controlling parameters on the system optical response are studied. Also, the results from our model are compared withthose based on the classical Beer–Lambert law (BLL) by fitting the corresponding absorption cross-sections, thus verifying that our model reproduces the experimentally measured RSA data. Finally, two different designs of plasmon-assisted OLs are introduced in Section 3.1, and their saturation intensities are compared with that of a thin film of a given RSA material.

2 RSA models

The band diagram of a material with RSA can be represented by an atomic four-level system with the Jablonski diagram shown in Figure 1A [18]. When light illuminates an RSA medium, the atom is excited from the ground singlet state S_0 to the first singlet state S_1 by absorbing a photon of the incident light, Figure 1B. The excited atom in S_1 can return to S_0 by radiating the same photon, or it can exhibit an intersystem crossing (ISC) relaxation to the first triplet state T_1. The atom at T_1 can either relax to S_0 or can be promoted to the second triplet state T_2 by absorbing a second photon if the incident light intensity is sufficient (Figure 1C). The additional absorption associated with the elevations of atoms from T_1 to T_2 is the origin of RSA. It can be thought of as an additional channel for absorption in addition to the ground-state absorption channel (singlet pair) due to the match in their energy gap, which is true

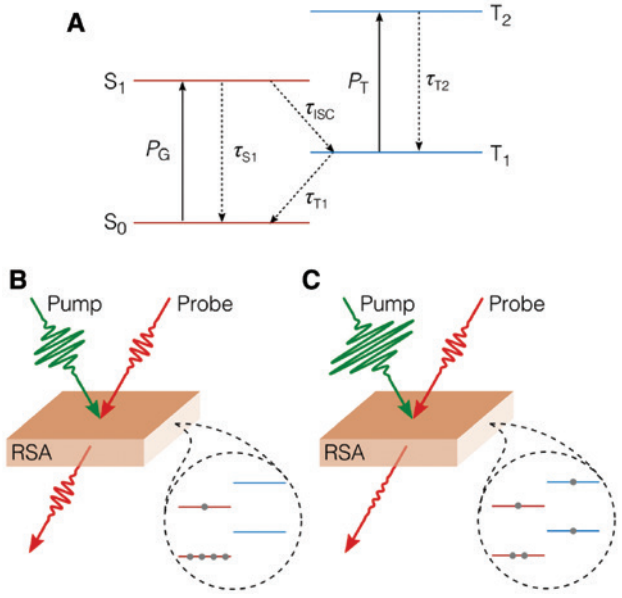

Figure 1: RSA physical mechanism.
(A) Jablonski diagram of an absorbing medium represented by a four-level atomic system. $S_{0,1}$ and $T_{1,2}$ represent the singlet and triplet states, respectively. (B) Linear regime: low-intensity pump with insufficient population in the lower triplet state. (C) Nonlinear regime: high-intensity pump with absorption taking place in the triplet states leading to RSA behavior.

for materials exhibiting RSA [4, 3]. For RSA to be efficient, a sufficient population of carriers should be transferred to T_1, which requires efficient ISC and a long triplet-state lifetime. Also, the absorption cross-section of the excited triplet states must be larger than that of the ground singlet state.

2.1 Beer–Lambert law

BLL is commonly used in spectroscopy and chemical analysis to relate the absorbance of a given absorbing material to its concentration in a host medium and the path length. The rate equations that model carrier kinetics at the different states are commonly employed to approximate the absorption coefficient of the materials [3, 19, 20]. Using the absorption coefficient with BLL, the intensity decay in uniformly absorbing samples can be found. Assuming three allowed relaxations, namely ISC from S_1 to T_1, relaxation form S_1 to S_0, and relaxation from T_1 to S_0, the rate equations governing the transitions inside the material are given by

$$\frac{\mathrm{d}N_{S_0}}{\mathrm{d}t}=\frac{N_{S_1}}{\tau_{S_1}}+\frac{N_{T_1}}{\tau_{T_1}}-N_{S_0}\frac{\sigma_G I}{\hbar\omega_0} \tag{1a}$$

$$\frac{\mathrm{d}N_{S_1}}{\mathrm{d}t}=-\frac{N_{S_1}}{\tau_{S_1}}-\frac{N_{S_1}}{\tau_{ISC}}+N_{S_0}\frac{\sigma_G I}{\hbar\omega_0} \tag{1b}$$

$$\frac{\mathrm{d}N_{T_1}}{\mathrm{d}t}=\frac{N_{S_1}}{\tau_{ISC}}-\frac{N_{T_1}}{\tau_{T_1}} \tag{1c}$$

where N_{S_0}, N_{S_1}, and N_{T_1} are the population densities in S_0, S_1, and T_1, respectively, and ω_0 is the frequency of the absorbed light. The time dependence of intensity in Eq. (2) is omitted for simplicity. The intensity of the light inside the sample can then be calculated using

$$\frac{\partial I}{\partial z}=-(N_{S_0}\sigma_G+N_{T_1}\sigma_T)I \tag{2}$$

where σ_G and σ_S are the ground-state and the singlet-state absorption cross-sections, respectively. Using this model, the time-dependent absorbance can be calculated, and the propagation of light intensity inside the sample can be straightforwardly obtained with a controlled accuracy and high efficiency even for tightly focused beams [19]. This approach, however, does not provide a material model that can be used to simulate more involved optical devices with dispersive or nonlinear materials and other multiphysics complications. Also, this simple, yet efficient, methodology does not allow access to the electric **E** or magnetic **H** vector fields and local population kinetics close to the device's nanostructured boundaries, and may not account for pumping dynamics following structured illumination. All these limitations are addressed with our full-wave multiphysics numerical framework, which includes a multilevel atomic model.

2.2 Four-level atomic system

As an example of a multilevel system, the atom or molecule of an RSA material is modeled using a four-level system with the Jablonski diagram shown in Figure 1A. The rate equations that govern all allowed transitions in a four-level system are given by

$$\frac{\partial N_{S_0}}{\partial t}=\frac{N_{S_1}}{\tau_{S_1}}+\frac{N_{T_1}}{\tau_{T_1}}-\frac{1}{\hbar\omega_0}\mathbf{E}\cdot\frac{\partial \mathbf{P}_G}{\partial t} \tag{3a}$$

$$\frac{\partial N_{S_1}}{\partial t}=-\frac{N_{S_1}}{\tau_{S_1}}-\frac{N_{S_1}}{\tau_{ISC}}+\frac{1}{\hbar\omega_0}\mathbf{E}\cdot\frac{\partial \mathbf{P}_G}{\partial t} \tag{3b}$$

$$\frac{\partial N_{T_1}}{\partial t}=-\frac{N_{T_1}}{\tau_{T_1}}+\frac{N_{S_1}}{\tau_{ISC}}+\frac{N_{T_2}}{\tau_{T_2}}-\frac{1}{\hbar\omega_0}\mathbf{E}\cdot\frac{\partial \mathbf{P}_T}{\partial t} \tag{3c}$$

$$\frac{\partial N_{T_2}}{\partial t} = -\frac{N_{T_2}}{\tau_{T_2}} + \frac{1}{\hbar\omega_0}\mathbf{E}\cdot\frac{\partial \mathbf{P}_T}{\partial t}. \tag{3d}$$

The population densities in the lower and upper singlet and triplet states, respectively, are N_{S_0}, N_{S_1}, N_{T_1}, and N_{T_2}. The total population, $N_d = N_{S_0} + N_{S_1} + N_{T_1} + N_{T_2}$, is conserved at all times, where N_d is the density of the absorbing atoms. The lifetime of state S_1 is $1/(1/\tau_{S_1} + 1/\tau_{ISC})$, where τ_{ISC} is the ISC lifetime. Lifetimes of the upper and lower triplet states are τ_{T_2} and τ_{T_1}. The term $\frac{1}{\hbar\omega_0}\mathbf{E}\cdot\frac{\partial \mathbf{P}_{ij}}{\partial t}$ represents the stimulated emission and absorption between levels $|i\rangle$ and $|j\rangle$.

The induced macroscopic polarizations due to the transitions satisfy the Lorentz ordinary differential equation, given by

$$\frac{\partial^2 \mathbf{P}_{ij}}{\partial t^2} + \gamma_{ij}\frac{\partial \mathbf{P}_{ij}}{\partial t} + \omega_0^2 \mathbf{P}_{ij} = \kappa_{ij}(N_j - N_i)\mathbf{E} \tag{4}$$

where γ_{ij} is the dephasing constant between levels $|i\rangle$ and $|j\rangle$. The energy spacing between the levels is $\Delta E_{S_{10}} \approx \Delta E_{T_{21}} = \hbar\omega_0$. The excitation term in Eq. (4) is proportional to the product of the local electric field and the difference in populations between the upper and the lower levels of this transition with a proportionality constant κ_{ij} where $ij \in \{G, T\}$. The coupling coefficient κ_{ij} represents the dipole matrix element between levels $|i\rangle$ and $|j\rangle$ and is given by $\kappa_{ij} = 2\omega_{ij}|\mu_{ij}|^2/\hbar = 6\pi\epsilon_0 c^3/\omega_{ij}^2\tau_{ij}$, where ϵ_0 and c are the free space permittivity and speed of light, respectively, and τ_{ij} is the decay time constant between levels $|i\rangle$ and $|j\rangle$ [21, 22]. The polarization densities are then coupled to the Maxwell equations through the electric flux

$$\nabla\times\mathbf{H}(t,\mathbf{r}) = \epsilon_0\epsilon_h\frac{\partial \mathbf{E}(t,\mathbf{r})}{\partial t} + \frac{\partial \mathbf{P}(t,\mathbf{r})}{\partial t} \tag{5}$$

$$\nabla\times\mathbf{E}(t,\mathbf{r}) = -\mu_0\frac{\partial \mathbf{H}(t,\mathbf{r})}{\partial t}, \tag{6}$$

and Eqs. (3–6) are solved simultaneously using a full-wave solver on a staggered Yee grid by applying the classical central finite-difference approximation to the spatial and time derivatives [23, 22]. The time-dependent electromagnetic fields are recorded and converted to the frequency domain using fast Fourier transform to obtain the transmission and reflection and, finally, the absorption.

3 Numerical details and results

A 1-μm-thick dielectric film is modeled using the proposed four-level atomic model in a host medium with refractive index 1. The lifetime and scattering rate parameters of the model are as follows: $\tau_{T_2} = 1$ ps, $\tau_{T_1} = 300$ ns, $\tau_{S_1} = 1$ ns, $\tau_{ISC} = 10$ PS, and $\gamma_G = \gamma_T = 10^{14}$. The density of the absorptive molecules is 0.3 mM (1.806×10^{17} cm^{-3}) and $\omega_0 = 2\pi/\lambda_0$, where λ_0 is 532 nm. The sample is illuminated with two plane-wave, normallyincident pulses separated by a short delay of 5 ps: a strong 1-ps pump pulse followed by a weak 50-fs probe. The probe fluence is fixed at 100 nJ/cm^2, while the fluence of the pump is varied from 10^{-3} to 10^2 μJ/cm^2 to study the nonlinear transmission and absorption of the thin RSA film. The wavelengths of both the pump and the probe are 532 nm. Transmission and reflection monitors are placed at at least half-wavelength separation from the sample and the source. Spatial grid size are set to 10 nm inside the RSA medium. Figure 2 shows the RSA behavior and time dynamics of the thin film. In Figure 2A, the transmission is linear (constant transmittance) at low input (pump) fluence and nonlinear at higher values; the saturation fluence for the RSA film is around 2.5 μJ/cm^2 in this example. The time dynamics of the system at two pump fluences of 10^{-2} and 50 μJ/cm^2 are depicted in Figure 2B–D. At 10^{-2} μJ/cm^2, well into the linear regime, the normalized ground-state population density is almost unity during all times and, consequently, the carrier build-up in the upper states is negligible (not shown). The time evolution of the macroscopic polarization densities of the ground (P_G) and excited triplet (P_T) states are shown in Figure 2B; as expected, P_T is almost negligible in this case. All polarizations are normalized to

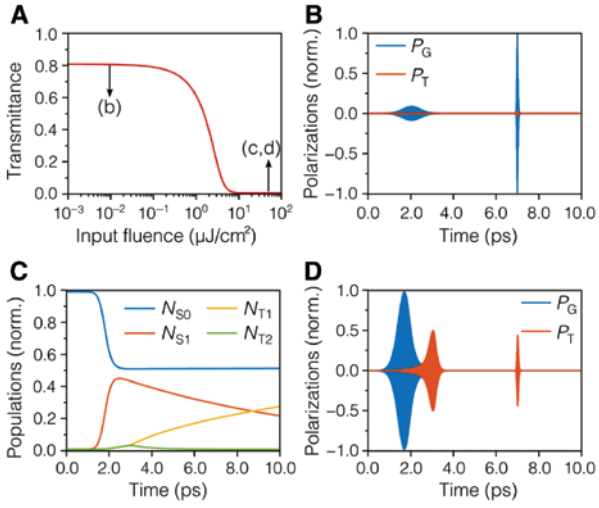

Figure 2: RSA behavior and time dynamics of the four-level system. (A) Transmittance vs. input fluence of a 1-μm film. (B) Induced polarization densities inside the RSA at 0.01 μJ/cm^2; polarizations are governed by the ground state, as the triplet state contribution in the linear regime is negligible (not shown). Nonlinear regime time dynamics for a pump fluence of 50 μJ/cm^2: (C) state densities and (D) polarizations.

the maximum value of P_G for clarity. Further, in the nonlinear regime with a pump fluence of 50 μJ/cm², the carrier dynamics (Figure 2C) shows depopulation of the ground state and increased build-up of triplet state density; hence, P_T starts to contribute to the material response (Figure 2D). We can clearly notice that the response of the system to the probe (around 7 ps) is completely dominated by P_T, which explains the enhanced absorption in this case.

Crossings of molecules from S_1 to T_1 requires undergoing a spin conversion in a process called ISC [24]. The efficiency of ISC is determined by the triplet quantum yield $\Phi_T = (1/\tau_{ISC} + 1/\tau_{S1})/\tau_{ISC}$. The faster the ISC rate $(1/\tau_{ISC})$, the higher the triplet quantum yield. Here, the effect of Φ_T on the system response is studied. The same sample as before is used while varying the ISC lifetimes to 1, 10, 100, and 1000 ps, corresponding to Φ_T of 0.999, 0.99, 0.909, and 0.5, respectively. Transmittance versus input fluence at the four different cases is depicted in Figure 3A. It can be noticed that for τ_{ISC} of 1, 10, and 100 ps, the material shows RSA behavior with increasing saturation fluence. However, at τ_{ISC} = 1 ns, the material acts as a saturable absorber. This matches the system dynamics very well. As seen in Figure 3B, at τ_{ISC} = 10 ps, the efficiency of the triplet quantum yield is high enough to allow for sufficient

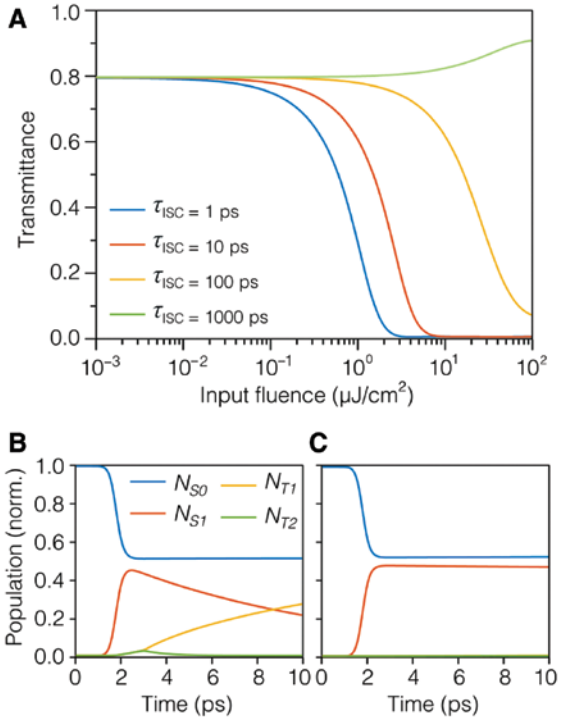

Figure 3: Effect of triplet quantum yield on the RSA efficiency. (A) Transmittance vs. pump fluence at four different values of τ_{ISC} = 1, 10, 100, and 1000 ps corresponding to Φ_T of 0.999, 0.99, 0.909, and 0.5, respectively. (B) and (C) the population time dynamics at 10 and 1000 ps at a pump energy of 50 μJ/cm².

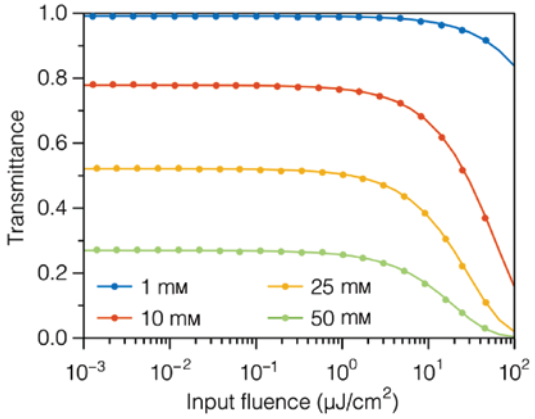

Figure 4: Transmittance vs. pump fluence using full-wave atomic system simulations (solid lines) vs. BLL (dotted lines) at different molecule densities.

population transfer to T_1 unlike at τ_{ISC} of 1 ns (Figure 3C), where the population density at T_1 is almost negligible and, as a result, the carrier density at S_1starts to saturate, leading to saturation of system absorption and hence to increased transmission (see the green line in Figure 3A).

Next, we compare the results of a 1-μm-thick RSA film with varying N_d using a four-level atomic model and the classical BLL. The lifetimes of the films are τ_{T_2} = 1 ps, τ_{T_1} = 1 μs, τ_{S_1} = 30 ns, and τ_{ISC} = 0.1 ns. The same lifetimes are used in both simulations while changing the absorption cross-sections to fit the two models. The fitted absorption cross-sections are $\sigma_G = 5.2\times10^{-20}\text{m}^{-3}$ and $\sigma_S = 9\times10^{-15}\text{m}^{-3}$. Figure 4 shows excellent agreement between the full-wave simulation (solid lines) and calculations based on the BLL equations (dotted lines). Generally, the BLL has been successfully used to fit experimental results [19, 20] of uniform samples. Having an excellent match with the BLL implies the ability of our model to fit and further utilize experimentally measured RSA transmission data. From Figure 4, the saturation intensity as well as the linear transmittance increases with decreasing molecular absorption densities, which suggests the use of thinner films with larger N_d in OLs device engineering.

3.1 Plasmon-enhanced optical limiters

Reducing the light intensity required for activating OLs is crucial for the expanding their area of application. For example, in protective goggles, OL devices should be activated at normal levels of the incoherent light illumination. From RSA materials standpoint, this translates to a very long triplet lifetime. Thus far, most of the development in this direction has been focused on developing materials

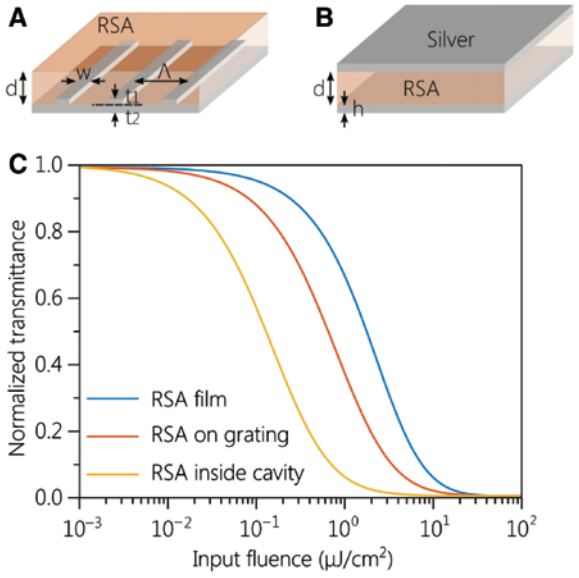

Figure 5: Enhancement of OLs using plasmonic structures. RSA thin film of 200 nm thickness (A) coated on top of a silver grating and (B) sandwiched between two thin silver layers. (C) Normalized transmittance vs. pump fluence for all three configurations: bare RSA thin film, the same film on top of a silver grating, and same RSA film between two thin silver layers.

with these favorable properties. In addition to this, here we use the multilevel material models developed for RSA to optimize optical limiting devices, where, due to the local field enhancement from plasmonic structures, the nonlinear response from RSA materials is further intensified. This way, the light intensity required for activating a given RSA device is greatly reduced. As a proof of concept, we design two plasmonic structures with an embedded RSA material to study the reduction in the saturation energy. Figure 5A shows the RSA material, with the same parameters as before, with thickness $d = 200$ nm on top of a silver grating. The bottom silver film is 20 nm thick (t_2), and the periodic ridges of the grating are 10 nm high (t_1) and 50 nm wide (w). The pitch of the grating structure (Λ) is 500 nm, and the optical properties of silver were obtained from [25]. The second configuration is depicted in Figure 5B, illustrating the same 200-nm RSA layer sandwiched between two silver films with thickness $h = 10$ nm. The geometrical parameters of the grating and the cavity are specifically chosen based on several parametric sweeps to maximize the linear transmission while reducing the saturation intensity. The spatial grid size isset to 10 nm inside the RSA medium and to 2.5 nm inside the silver. The linear transmittance is 0.93 in the case of bare RSA film, 0.46 in the case of RSA film on a grating, and 0.68 in the case of the RSA layer inside a cavity-like structure. Figure 5C shows the normalized transmittance as a function of the input fluence of all three structures: a bare 200-nm RSA, the 200-nm RSA film on a grating, and the 200-nm RSA inside a cavity-like structure. The transmittance in each case is normalized to its maximum for more straightforward comparison. As observed in Figure 5C, the saturation intensity for the bare RSA film is 2.651 μJ/cm², for the RSA film on a grating is 1.019 μJ/cm², and for the RSA film in a cavity-like structure is 0.2006 μJ/cm². This is a 2.6-fold reduction in the saturation intensity for the grating structure and 13.2-fold reduction in the cavity configuration. The method is also successfully verified with a custom solver built on the finite-element time-domain method, FETD in COMSOL Multiphysics by combining the Wave Optics Module with additional ODEs in the time-domain [26].

4 Conclusion

A 3D full-wave analysis of the RSA devices with the ability to model light–matter interaction based on rate equations that could include non-paraxial structured beams and complex photonic structures with diverse material composition has been presented and validated. The results of the proposed model agree well with the classical Beer–Lambert equation used to fit the experimental RSA data while also providing a comprehensive physical understanding of the field and carrier dynamics within the absorbing material. Examples of two plasmon-enhanced OLs that utilize the field enhancement to lower the saturation intensity were proposed. More than one order of magnitude reduction of the light fluence required to activate the RSA structures with plasmonic elements was achieved. Using our technique, the numerical modeling and optimization of the devices with complex micro- and nano-structured materials and illumination are made possible, which opens up new opportunities to explore high-sensitivity, low-threshold OLs beyond homogeneous RSA light–matter limitations. Future work will include other important effects into our model, such as the Pauli exclusion principle, for more accurate representation of RSA materials.

Acknowledgment: The authors appreciate the reviewers' positive feedback and invaluable comments on the manuscript.

Funding: The authors acknowledge the financial support by DARPA/DSO Extreme Optics and Imaging (EXTREME) Program, Award HR00111720032, Funder Id: http://dx.doi.org/10.13039/100006502.

References

[1] Hollins RC. Materials for optical limiters. Curr Opin Solid State Mater Sci 1999;4:189–96.

[2] Kiran PP, Shivakiran Bhaktha BN, Rao DN, De G. Nonlinear optical properties and surface-plasmon enhanced optical limiting in Ag–Cu nanoclusters co-doped in SiO_2 Sol-Gel films. J Appl Phys 2004;96:6717–23.

[3] Li C, Zhang L, Wang R, Song Y, Wang Y. Dynamics of reverse saturable absorption and all-optical switching in C60. JOSA B 1994;11:1356–60.

[4] Srinivas NN, Rao SV, Rao DN. Saturable and reverse saturable absorption of Rhodamine B in methanol and water. JOSA B 2003;20:2470–9.

[5] Tutt LW, McCahon SW. Reverse saturable absorption in metal cluster compounds. Opt Lett 1990:15:700–2.

[6] Gurudas U, Brooks E, Bubb DM, Heiroth S, Lippert T, Wokaun A. Saturable and reverse saturable absorption in silver nanodots at 532 nm using picosecond laser pulses. J Appl Phys 2008;104:073107.

[7] Blau W, Byrne H, Dennis WM, Kelly JM. Reverse saturable absorption in tetraphenylporphyrins. Opt Commun 1985;56:25–9.

[8] Sun X, Xiong Y, Chen P, et al. Investigation of an optical limiting mechanism in multiwalled carbon nanotubes. Appl Opt 2000;39:1998–2001.

[9] Ouyang Q, Yu H, Wu H, Lei Z, Qi L, Chen Y. Graphene/MoS_2 organic glasses: fabrication and enhanced reverse saturable absorption properties. Opt Mater 2013;35:2352–6.

[10] Cheng Z, Li H, Shi H, Ren J, Yang QH, Wang P. Dissipative soliton resonance and reverse saturable absorption in graphene oxide mode-locked all-normal-dispersion Yb-doped fiber laser. Opt Exp 2015;23:7000–6.

[11] Hirata S, Totani K, Yamashita T, Adachi C, Vacha M. Large reverse saturable absorption under weak continuous in coherent light. Nat Mater 2014;13:938.

[12] Hirata S, Vacha M. Large reverse saturable absorption at the sunlight power level using the ultralong lifetime of triplet excitons. J Phys Chem Lett 2017;8:3683–9.

[13] Varin C, Bart G, Emms R, Brabec T. Saturable Lorentz model for fully explicit three-dimensional modeling of nonlinear optics. Opt Exp 2015;23:2686–95.

[14] Hill SC, Videen G, Sun W, Fu Q. Scattering and internal fields of a microsphere that contains a saturable absorber: finite-difference time-domain simulations. Appl Opt 2001;40:5487–94.

[15] Mock A. Modeling passive mode-locking via saturable absorption in graphene using the finite-difference time-domain method. IEEE J Quantum Electron 2017;53:1–10.

[16] Lumerical Inc. http://www.lumerical.com/tcad-products/fdtd/.

[17] Trieschmann J, Xiao S, Prokopeva LJ, Drachev VP, Kildishev AV. Experimental retrieval of the kinetic parameters of a dye in a solid film. Opt Exp 2011;19:18253–9.

[18] Yang GY, Hanack M, Lee YW, Chen Y, Lee MK, Dini D. Synthesis and nonlinear optical properties of fluorine-containing naphthalocyanines. Chem–Eur J 2003;9:2758–62.

[19] Kovsh DI, Yang S, Hagan DJ, Van Stryland EW. Nonlinear optical beam propagation for optical limiting. Appl Opt 1999;38:5168–80.

[20] Lepkowicz R, Kobyakov A, Hagan DJ, Van Stryland EW. Picosecond optical limiting in reverse saturable absorbers: a theoretical and experimental study. JOSA B 2002;19:94–101.

[21] Nagra AS, York RA. FDTD analysis of wave propagation in nonlinear absorbing and gain media. IEEE Trans Antennas Propag 1998;46:334–40.

[22] Chang S, Taflove A. Finite-difference time-domain model of lasing action in a four-level two-electron atomic system. Opt Exp 2004;12:3827–33.

[23] Yee K. Numerical solution of initial boundary value problems involving Maxwell's equations in isotropic media. IEEE Transactions Antennas Propag 1966;14:302–7.

[24] Masters BR. Principles of fluorescence spectroscopy. J Biomed Opt 2008;13:029901.

[25] Johnson PB, Christy RW. Optical constants of the noble metals. Phys Rev B 1972;6:4370.

[26] COMSOL, Inc. https://www.comsol.com/wave-optics-module.